



# Mechanistic insights into photo-current enhancement in photo-active SrTiO<sub>3</sub> heterojunctions under UV illumination

Alexander Schmid<sup>\*</sup>, Ludwig Enzlberger, Jürgen Fleig

*Institute of Chemical Technologies and Analytics, TU Wien, Getreidemarkt 9, Vienna A-1060, Austria*

## ARTICLE INFO

### Keywords:

Strontium titanate  
Photo-electrochemistry  
Photo-current  
Resistance degradation

## ABSTRACT

Photo-active heterojunctions were prepared by growing thin La<sub>0.9</sub>Sr<sub>0.1</sub>CrO<sub>3-δ</sub> films on SrTiO<sub>3</sub> (STO) single crystals substrates via pulsed laser deposition. The photo-electrochemical characteristics of these heterojunctions under UV illumination were investigated by DC measurements and electrochemical impedance spectroscopy (EIS). Under UV illumination, the photo-current produced by these junctions increases over time by almost an order of magnitude to 1 to 2 mA cm<sup>-2</sup> at 350 °C. Two effects governing this increase can be distinguished: A first process, independent of the surrounding atmosphere, is related to a stoichiometry polarization of the STO single crystal upon current flow. A second process is highly sensitive to contaminants in the surrounding atmosphere and is strongly accelerated in pure, synthetic atmospheres. We suggest that it is related to photo-oxidation of the STO single crystal. EIS revealed that both processes result in a decrease of both the electronic transport resistance through the STO single crystal and, to a lesser degree, the space charge resistance of the photo-active junction. Operando EIS under illumination and with DC bias was used to record the cells' photo-power characteristics and identify individual loss processes. Owing to the illumination induced strong increase of the STO single crystal conductivity, the photo-currents of such enhanced cells are limited by the space charge resistance.

## 1. Introduction

Transforming our energy economy to a carbon-neutral, sustainable cycle imposes great challenges on energy production technologies. This is exacerbated by an increasing electrification and digitalization and the ever more diverse environments, where electrical energy is desired. Photo-voltaic (PV) cells are particularly attractive for power generation, converting abundant solar radiation directly into electrical energy. Ambient temperature PV cells are well established and produced in large volumes, mostly based on silicon [1–3]. In contrast, ceramic PV cells are far less developed. They have been realized based on different chalcogenides, e.g. MoS<sub>2</sub> or CdTe [4,5] or oxides such as Cu<sub>2</sub>O, ZnO, TiO<sub>2</sub> or BiFeO<sub>3</sub> [6–12]. Also SrTiO<sub>3</sub> (STO) is a highly interesting oxide in this context, since it exhibits a multitude of light-induced effects [13] such as photo-chromism [14,15], photo-conductivity [16,17] and photo-oxidation [15,18–21]. Furthermore, STO forms photo-active heterojunctions with multiple materials. For example, interfaces between Nb: SrTiO<sub>3</sub> and either YBa<sub>2</sub>Cu<sub>3</sub>O<sub>7-δ</sub> [22], La<sub>0.5</sub>Ca<sub>0.5</sub>MnO<sub>3-δ</sub> [23] or Cu<sub>2</sub>O [24] generate photo-voltages upon illumination, mostly at room temperature. Additionally, heterojunctions between undoped or Fe doped

STO single crystals and thin ceramic oxide (La<sub>0.9</sub>Sr<sub>0.1</sub>CrO<sub>3-δ</sub>(LSCr), La<sub>x</sub>Sr<sub>1-x</sub>MnO<sub>3-δ</sub>, La<sub>x</sub>Co<sub>1-x</sub>MnO<sub>3-δ</sub> (LSC), LaCrO<sub>3</sub>, La<sub>x</sub>Sr<sub>1-x</sub>Cr<sub>y</sub>Mn<sub>1-y</sub>O<sub>3-δ</sub>) or metal (Au, Pt) films generate photo-voltages up to 1.1 V even at elevated temperatures (200 to 400 °C) [25,26]. Moreover, the photo-current produced by such cells was shown to increase over time in operation [25].

In this study, we investigate the photo-electrochemical properties of cells based on heterojunctions between STO single crystals and LSCr thin film photo-electrodes. First, DC measurements and electrochemical impedance spectroscopy (EIS) are employed to quantitatively analyze the strongly atmosphere-dependent increase of the photo-current under UV illumination and identify the mechanistic processes responsible for this self-enhancement. We distinguish two processes — a first process is related to stoichiometry polarization of the STO single crystal and a second process is likely caused by photo-oxidation. Together, these processes cause an increase of the photo-current by almost an order of magnitude, resulting in short circuit currents of 1 to 2 mA cm<sup>-2</sup> at 350 °C for fully self-enhanced cells. Second, we analyze the power characteristics of such self-enhanced cells and separate individual loss processes. Due to the strong increase of the STO bulk conductivity upon UV

<sup>\*</sup> Corresponding author.

E-mail address: [alexander.e164.schmid@tuwien.ac.at](mailto:alexander.e164.schmid@tuwien.ac.at) (A. Schmid).

<https://doi.org/10.1016/j.ssi.2024.116469>

Received 7 November 2023; Received in revised form 11 January 2024; Accepted 16 January 2024

Available online 24 January 2024

0167-2738/© 2024 The Author(s). Published by Elsevier B.V. This is an open access article under the CC BY license (<http://creativecommons.org/licenses/by/4.0/>).

illumination, the associated transport resistance becomes negligible and the cell's output is limited by the resistive properties of the photo-active space charge region.

## 2. Experimental

### 2.1. Sample preparation

LSCr powder was prepared via Pechini's route: Metal precursors (Cr (NO<sub>3</sub>)<sub>3</sub>, La<sub>2</sub>O<sub>3</sub>, SrCO<sub>3</sub>, purity >99.995%) were dissolved in dilute nitric acid and citric acid was added in a molar ratio of 1:1 with respect to total cations. The solution was stirred at 90 °C for two hours and afterwards evaporated until completely dry. The dry foam was then further heated until self ignition and combustion occurred and subsequently calcined in air at 850 °C for 2 h. This powder was pressed (71 MPa) and sintered in air for 12 h at 1200 °C to produce a deposition target for pulsed laser deposition (PLD).

STO single crystals (10 × 10 × 0.5 mm<sup>3</sup>, (100) orientation, polished on one flat side) were used as substrates for preparation of high temperature photo-voltaic cells. Prior to thin film deposition, the crystals were cleaned in an ultrasonic bath in Extran, water and ethanol and afterwards annealed at 900 °C for 1 h in 1.5 Pa O<sub>2</sub> inside the PLD chamber. LSCr thin films (100 nm thickness) were grown on the polished side by PLD, using a laser pulse energy of 110 mJ (1 J cm<sup>-2</sup>), a substrate temperature of 700 °C and an oxygen pressure of 1.5 Pa. Pt current collector grids (100 nm thickness, 35 μm mesh width, 15 μm strip width) were deposited on top of the LSCr films by lift-off photo-lithography and direct current magnetron sputtering. Porous Pt counter electrodes were prepared on the unpolished flat side by brushing Pt paste and baking at 400 °C in air. Fig. 1a shows a sketch of the resulting sample structure.

### 2.2. Photo-electrochemical characterization

Samples were mounted and electrically contacted in an alumina sample holder enclosed in a tube of fused silica and placed inside a tube furnace, see Fig. 1b. Samples were illuminated by UV light via a fused silica rod (1 cm diameter) serving as light guide, placed through a circular cut-out in the sample holder. An LED lamp (LZ4 LuxiGen UV LED Emitter, LED Engin, USA) with a nominal power of 2.9 W and a

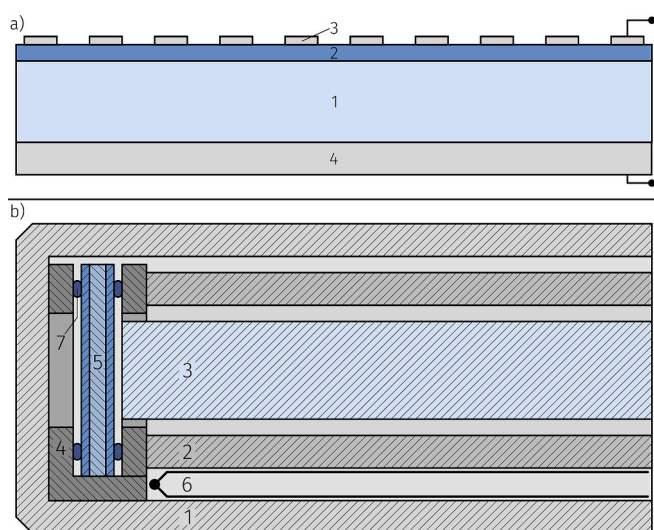


**Fig. 1.** (a) Schematic of the high temperature (HT)-PV cell consisting of STO single crystal substrate (1), LSCr photo-electrode (2), Pt current collector (3) and porous Pt counter electrode (4). (b) Measurement stage used for Photo-electrochemical characterization consisting of outer silica tube (1), inner silica tube (2), silica light guide (3), alumina sample holder (4), sample (5), thermocouple (6) and electrical contacting (7).

wavelength of 365 nm was used as UV light source, resulting in a UV power density of 70 mW cm<sup>-2</sup> at the sample. DC measurements were done using a Keithley 2000 digital multimeter and a Keithley 2600 source measure unit. Impedance measurements were performed by means of a Novocotrol Alpha-A impedance analyzer with PotGal interface using an AC voltage of 10 mV. Prior to electrochemical measurements, samples were allowed to equilibrate with the measurement atmosphere for at least 6 h.

Pristine, as prepared, samples were first characterized by impedance spectroscopy without illumination, followed by a measurement of the open circuit voltage (OCV) under intermittent illumination. Then, the short circuit current (SCC) was recorded under intermittent illumination for multiple illumination cycles and impedance spectra were recorded in between the illumination phases. After this self-enhancement, the OCV was measured again and lastly, impedance spectra were recorded without illumination. These time dependent measurements were performed at 350 °C in both ambient air and in pure, synthetic air (80% N<sub>2</sub>, 20% O<sub>2</sub>, both >99.999%). For ambient air measurements the setup was left open to the surrounding atmosphere without imposing a gas flow; for measurements in synthetic air a flow of 20 cm<sup>3</sup> min<sup>-1</sup> was used. Afterwards, impedance spectra were recorded at 250 °C, 300 °C, 350 °C and 400 °C under UV illumination in synthetic air and with DC bias voltages between 0 V and the respective open circuit voltages.

Please note: All voltages and currents reported are with respect to the LSCr photo-electrode. For example, a positive voltage means that the LSCr electrode is at a more negative potential than the counter electrode, and positive currents mean that electrons in the external circuit flow from the LSCr photo-electrode to the counter electrode, respectively.

## 3. Time dependent photo-voltage and current

Fig. 2 displays the OCV of several nominally identical high temperature (HT)-PV cells based on STO single crystal substrates and LSCr photo-electrodes under intermittent UV illumination. Upon illumination the OCV reaches a constant value of 1.15 ± 0.02 V V, see Fig. 2a. Slight increases or decreases within the first 3 to 5 min in the beginning are in accordance with literature but beyond the scope of this work. The

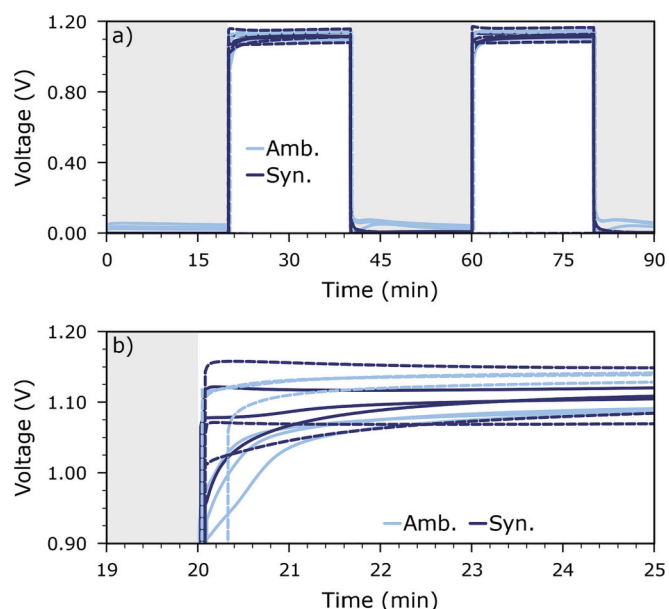


**Fig. 2.** Time evolution of the open circuit photo-voltages of three nominally identical samples in ambient air and three nominally identical samples in synthetic air under intermittent UV illumination at 350 °C (a) and magnification of the onset of photo-voltage after switching on the illumination (b). The gray shaded areas indicate phases without illumination.

measurement atmosphere — either ambient air or a pure O<sub>2</sub>/N<sub>2</sub> mixture — had neither a strong effect on the final value of the OCV nor on the time it took to reach it, see the magnification in Fig. 2b. Furthermore, the OCV did not show any appreciable variation between different, identically prepared, samples. This voltage is significantly higher than that produced by similar cells without LSCr photo-electrode (50 to 400 mV for 10 to 100 nm Pt), i.e. cells utilizing the STO-Pt space charge [25,27].

On the other hand, the short circuit current (SCC) does exhibit a distinctly different time dependence in pure synthetic air and in ambient air and, moreover, shows significant variation between different samples, see Fig. 3. In ambient air, the SCC is initially very low (in the range of 1 to 5  $\mu\text{A cm}^{-2}$ ) but increases to  $110 \pm 60 \mu\text{A cm}^{-2}$  within 20 to 30 min, see Fig. 3a and its magnification in Fig. 3b. This first increase is followed by a much slower increase of the SCC which persists over much longer timescales and ultimately reaches a final value of  $770 \mu\text{A cm}^{-2}$  after about 150 h. Interruption of the illumination leads to a very fast drop of the current. The SCC again increases rapidly for 20 to 30 min once illumination is restored, reaching approximately the SCC present prior to removing the illumination. This increase is then again followed by a much slower increase of the SCC.

In pure synthetic air, the SCC initially also increases for 20 to 30 min, but, in contrast to the case of ambient air, this first increase is not followed by a second, slower one. Rather, the SCC remains virtually constant afterwards at  $1.5 \pm 0.3 \text{ mA cm}^{-2}$ , see Fig. 3c. Furthermore, the currents reached after this initial rapid increase are comparable to the final SCC reached in ambient air after 150 h. After interrupting the illumination, the SCC again increases for 20 to 30 min to its value prior

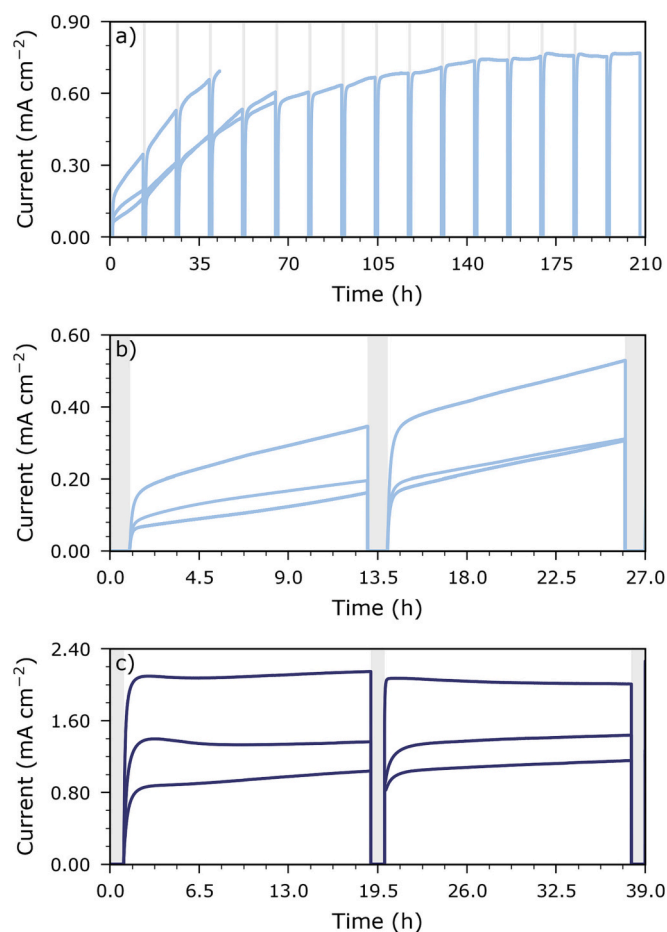


**Fig. 3.** Short circuit photo-currents in ambient air (a, and magnified in b) and in pure, synthetic air (c) under intermittent UV illumination at 350 °C. Three nominally identical samples are shown for both atmospheres. The gray shaded areas indicate phases without illumination.

to the interruption, and afterwards remains constant. Please note: This increase of the photo-current occurs only during illumination and current flow. In contrast, illumination without current flow, i.e. under open circuit conditions, does not affect the measured photo-current.

These data suggest that two separate processes with very different characteristic times are responsible for the time dependent increase of the SCC:

- The first process takes place within 20 min and 30 min at 350 °C and is not affected by the measurement atmosphere. The associated changes do not fully persist in the dark and therefore the current increase reoccurs after every interruption of the illumination.
- The second process, however, strongly depends on the measurement atmosphere. In ambient air it is very slow (150 h), whereas in pure, synthetic air it is at least as fast as the first process (<20 min) and thus cannot be resolved. The effects causing this current increase, however, persist even after removing illumination.

From the distinctly different atmosphere dependence of the two process we may infer that the first process might be a bulk process whereas the second process likely involves some interaction with the atmosphere, e.g. oxygen exchange. However, before we discuss a mechanistic model of this effect, we consider the results of electrochemical impedance spectroscopy measurements on these samples.

#### 4. Electrochemical impedance spectroscopy

Impedance spectra were recorded before and after illumination to complement the DC experiments and to investigate the effect of illumination on the individual resistance contributions. Fig. 4a shows representative impedance spectra recorded at 350 °C on two pristine cells in ambient air and in pure synthetic air. Spectra recorded on nominally identical samples exhibited the same trends, however, with different absolute values, consistent with the significant scatter in SCC between samples. Average parameters extracted from impedance recorded on multiple cells are listed in the supporting information S1.

In both atmospheres, spectra exhibit a high frequency semicircle, a strongly depressed shoulder at intermediate frequencies and a dominant arc at low frequencies. The high frequency semicircle is of equal size in both atmospheres, whereas the medium and low frequency features are larger in ambient air. These spectra are similar to impedance spectra discussed in previous publications, and are interpreted accordingly [25,26]. Quantitative parameters were extracted from these spectra by fitting the data to an equivalent circuit model consisting of three elements in series, corresponding to the three distinct features at high, medium and low frequencies. The high frequency feature was modelled by a parallel R-C element, except for the fully enhanced cell in synthetic air, where only a resistor was used. The medium and low frequency features were each modelled by an R-CPE element, where the constant phase element (CPE) represents a non-ideal capacitor with impedance  $Z_{\text{CPE}} = T^{-1}(i\omega)^{-P}$ ; a  $P$  value of 1 corresponds to an ideal capacitor.

The high frequency semicircle is attributed to the electronic transport resistance of the STO single crystal in parallel to its dielectric capacitance. The extracted conductivity is  $2.5 \times 10^{-7} \text{ S cm}^{-1}$  and the relative permittivity of 182 closely matches that reported for bulk STO at 350 °C [28,29]. The intermediate frequency feature is attributed to the counter electrode. The low frequency arc is attributed to the space charge at the heterojunction between LSCr and STO, which is responsible for charge carrier separation and photo-voltage generation under illumination. In this space charge region, the main charge carriers (electron holes) are depleted by many orders of magnitude, leading to a highly resistive interface which dominates the total resistance. In contrast, the LSCr-Pt interface does not form a pronounced space charge region, as both materials have high charge carrier densities. (The electron hole concentration in LSCr is about  $1.6 \times 10^{21} \text{ cm}^{-3}$ .)

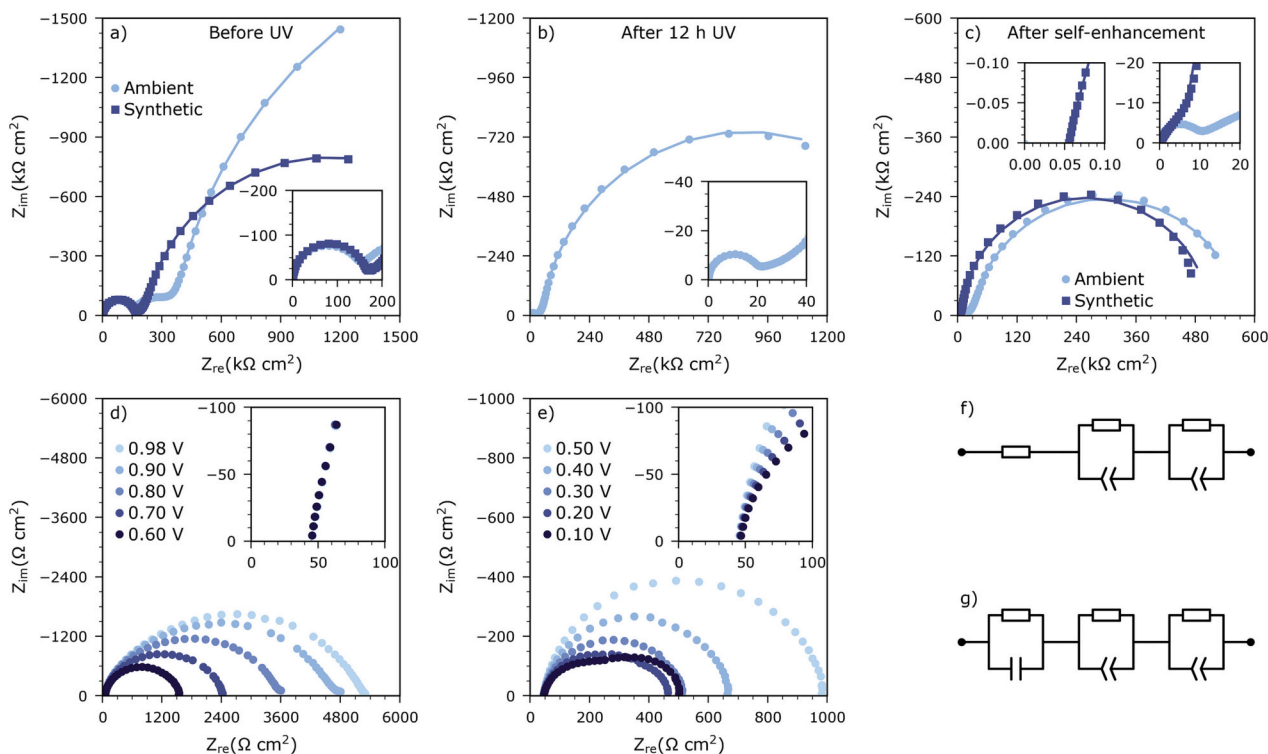


**Fig. 4.** Impedance spectra of STO single crystal based HT-PV cells recorded at 350 °C in ambient and pure, synthetic air before illumination (a), after a first illumination phase (12 h) in ambient air (b) and after the self-enhancement in ambient and synthetic air (c). Impedance under illumination and different loads for a fully self-enhanced cell in synthetic air (d, e). Markers represent measured data points, solid lines are fits to the equivalent circuit models: (f) for the synthetic air spectrum in (c), (g) for all other spectra.

**Fig. 4b** displays a spectrum recorded in ambient air after the first illumination phase, i.e. in a state where the SCC increase is still in large parts due to the first, atmosphere independent process discussed above, cf. **Fig. 3a**. Qualitatively it is very similar to the pristine spectrum, except that the resistances of all three features are markedly lower. **Fig. 4c** shows impedance spectra recorded without illumination after the self-enhancement was completed, i.e. once a stable SCC was reached. Again, all features exhibit a distinctly lower resistances compared to the pristine state. The high frequency arc shows the most drastic decrease, from 160 kΩ cm<sup>2</sup> to 10 kΩ cm<sup>2</sup> in ambient air. **Fig. 4c** also displays a spectrum measured after the self-enhancement in synthetic air which reveals an even stronger decrease of the bulk resistance to 54 Ω cm<sup>2</sup>. This drastic decrease by a factor of 3000 also causes the peak frequency of the high frequency feature to increase beyond our experimentally accessible range, and we only observe an intercept on the real axis. In synthetic air, the intermediate frequency resistance decreases by a factor of 8, and the low frequency resistance decreases only by a factor of 3.7. The capacitances of all features in both atmospheres, on the other hand, are virtually unchanged after the self-enhancement.

**Fig. 4d** and **e** show impedance spectra recorded on a fully self-enhanced cell but still under illumination in synthetic air and with different bias voltages between 0.98 V (close to open circuit conditions) and 0.1 V (close to short circuit conditions). Under illumination the high frequency intercept is slightly lower than without illumination. This is most likely a temperature effect due to the UV illumination (approximately 5 to 10 °C), but may also include a photo-conductivity contribution. The high frequency resistance does not change with voltage, consistent with its interpretation as an ohmic transport resistance through the STO single crystal. At intermediate to low frequencies, we find a strongly depressed feature which in some cases seems to separate into two arcs (e.g. for 0.1 V and 0.2 V). A reliable separation into counter electrode and photo-active electrode, however, is not possible, and thus we only consider the entire resistance, determined by subtracting its

high and low frequency real axis intercepts. This resistance is distinctly voltage-dependent, consistent with our interpretation as a space charge resistance and therefore also denoted as such. It is by a factor of 100 to 1000 lower than without illumination, depending on the applied voltage. **Fig. 5** displays the extracted STO transport and space charge resistances at different temperatures as a function of cell voltage in a temperature range from 250 to 400 °C.

## 5. Power characteristics and loss processes

**Fig. 6** displays exemplary current vs. voltage and current vs. power characteristics of one STO-LSCr cell in synthetic air, after self-enhancement. Mean values over multiple such cells are listed in the supporting information S2. At 400 °C, the cell produced a maximum power of 170 mW cm<sup>-2</sup> at 0.6 mA cm<sup>-2</sup> and 0.3 V. To analyze the origin of the internal cell losses and identify the limiting process, we consider the (differential) resistances of bulk and space charge under illumination, determined by EIS (**Fig. 5**). We model the cell as an ideal (i.e. load independent) voltage source in series with the (load independent) bulk transport resistance and the load dependent space charge resistance; the corresponding circuit is displayed in **Fig. 7d**.

More specific, we calculate the overpotentials due to the electronic transport through the STO single crystal (bulk) and through the space charge region by integrating the corresponding differential resistances determined by EIS over the current, i.e.

$$\eta_{\text{STO}}(I) = \int_0^I R_{\text{STO}} di, \quad (1)$$

and

$$\eta_{\text{SC}}(I) = \int_0^I R_{\text{SC}} di. \quad (2)$$

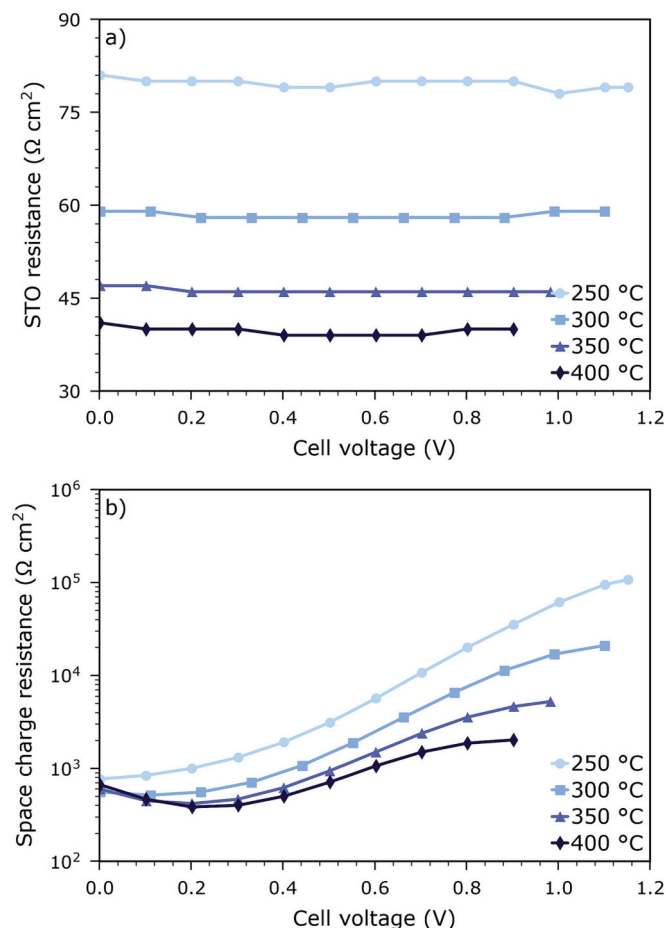


Fig. 5. High frequency STO transport resistance and low frequency space charge resistance of a fully self-enhanced PV cell, extracted from impedance spectra measured at 250 °C, 300 °C, 350 °C and 400 °C under illumination as a function of cell voltage.

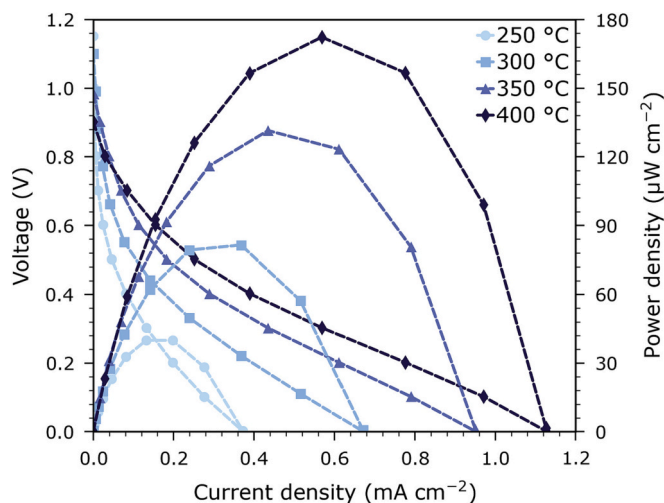


Fig. 6. Current vs. voltage and current vs. power curves of an STO HT-PV cell under UV illumination at different temperatures in synthetic high purity air.

Fig. 7 displays these overpotentials as a function of current density and temperature. Adding the resulting overpotentials to the cell voltage under load yields approximately the open circuit voltage, confirming the consistency of this analysis, see Fig. 7c. Differences between this

calculated OCV and the measured OCV are likely the result of integration over a limited number of data point leading to an accumulation of errors.

The overpotentials attributed to the electron transport through the STO single crystal show a linear increase with voltage, consistent with the ohmic nature of the STO transport resistance. The corresponding bulk conductivity of the photo-oxidized STO is between  $6.3 \times 10^{-4} \text{ S cm}^{-1}$  at 250 °C and  $1.3 \times 10^{-3} \text{ S cm}^{-1}$  at 400 °C. These conductivities are much larger than expected for STO equilibrated in air but in accordance with our assumption of a strongly increased electron hole concentration due to photo-oxidation, see model below. Furthermore, the resistance slightly decreases with increasing temperature — the corresponding activation energy is between 0.15 eV and 0.25 eV. Since the mobility of the main charge carrier (electron holes) decreases with temperature [30], this suggests a thermally activated increase in mobile electron hole concentration. The space charge overpotentials, on the other hand, exhibit an almost exponential relation between current and overpotential. Over the entire parameter space, this space charge overpotential dominates the total internal losses. This remaining space charge overpotential is closely tied to the characteristics of the space charge region and is thus an intrinsic property of the specific LSCr-STO interface. These results have an important practical implication for optimizing the performance of such STO HT-PV cells: Namely, the performance gains expected from eliminating the STO transport resistance, e.g. by replacing the single crystal with a thin layer, are rather marginal since anyway the space charge determines the losses. In the most optimistic case, a performance increase of about 5% is expected. Only by changes of the LSCr layer and thus the interface we may further improve the corresponding PV cell.

## 6. Mechanistic discussion of the self-enhancement

Lastly, we attempt a mechanistic explanation of the self-enhancement of the HT-PV cells under operation. Time resolved DC measurements revealed that two processes are responsible for the self-enhancement: One atmosphere independent process (I) and one being strongly atmosphere dependent (II). EIS has shown that each of these processes leads to a reduction of both major contributions to the internal cell resistance — the STO bulk transport resistance and the space charge resistance. Of these, the space charge resistance is the dominant resistance, also under illumination and current flow, and thus it is the limiting factor for cell performance.

However, for the discussion of the self-enhancement we have to keep in mind that the STO bulk transport resistance and the space charge resistance are not independent. Rather, according to simple models for depletion type space charges, the resistivity of the space charge region scales linearly with the resistivity of the bulk, for otherwise similar parameters. Therefore, any changes in STO bulk resistivity also translate to changes in the space charge resistance [31]. Modifications of the entire STO bulk most likely takes more time than modifications of only the space charge zone, due to vastly greater spatial extent of the crystal. We may thus end up in a situation, where changes of the STO bulk govern the time dependence of the self-enhancement via the indirect effect of the STO bulk resistivity on the space charge resistivity, despite the fact that the resistance of the space charge itself is still the limiting factor for device performance. Based on this premise, we now discuss the specific processes that may lead to a decrease of the STO bulk resistivity, and thus indirectly cause the self-enhancement of the HT-PV cells.

Initially, under illumination the not-yet-enhanced STO bulk resistance is much greater than the resistance of the illuminated space charge region. Thus, under short circuit conditions, the photovoltage predominantly drops across the bulk of the STO crystal. (After self-enhancement the situation is different, as the resistance of the fully enhanced cells under illumination is dominated by the space charge resistance.) Since ionic (oxygen vacancy) motion is at least partly blocked at the electrodes, this unavoidably causes a stoichiometry polarization, i.e. the

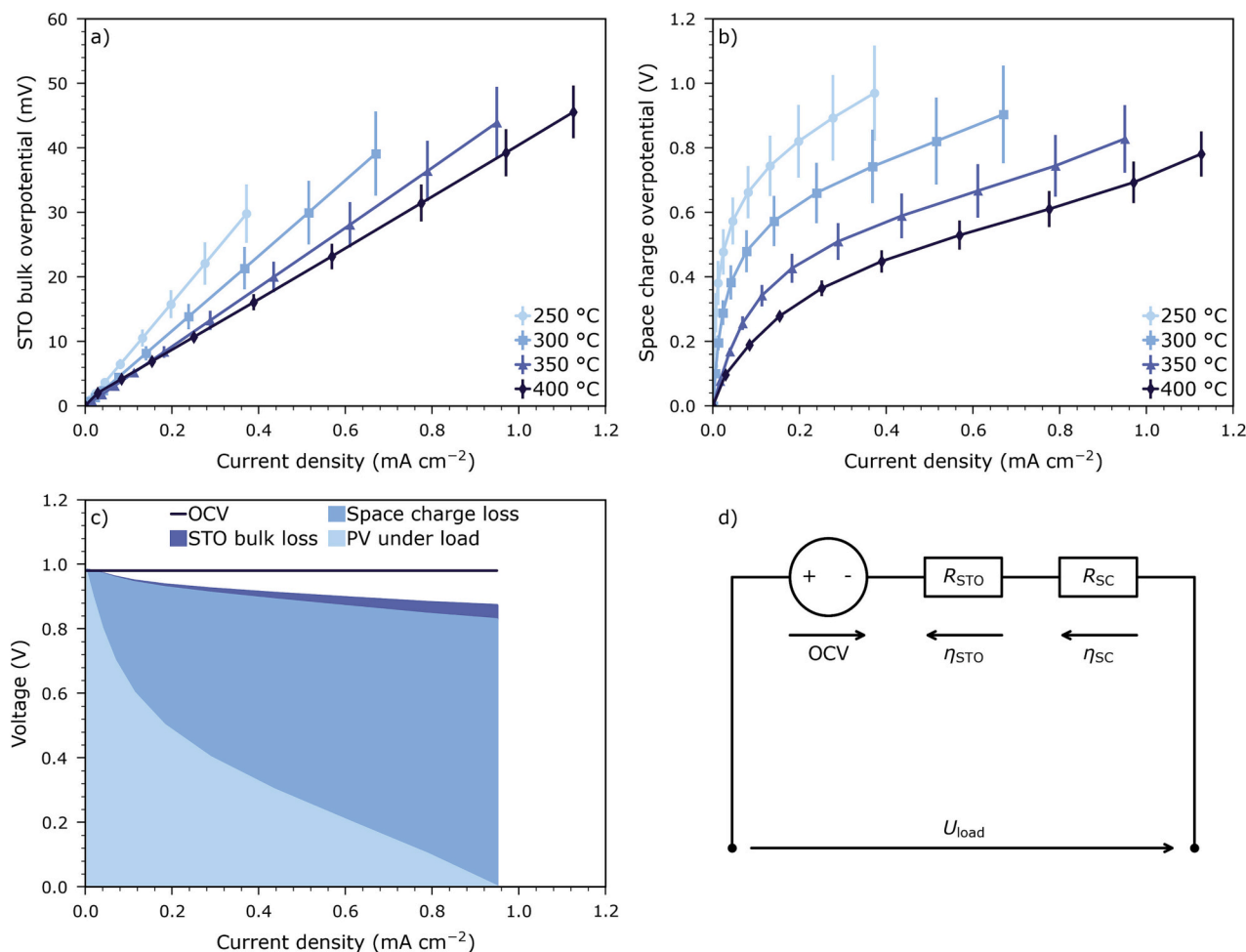


**Fig. 7.** Individual overpotential contributions due to electron transport in the STO bulk (a) and space charge resistances (b) at different temperatures as a function of current density, calculated from the resistances shown in Fig. 5. The errors are estimated by subtracting these overpotentials and the measured photo-voltage under load from the measured OCV, see (c), which displays the individual parts of the cell voltage under load — output photo-voltage, bulk transport loss and space charge loss. The corresponding circuit model is shown in (d).

buildup of an oxygen chemical potential (and thus also charge carrier concentration) gradient across the entire STO crystal [25,32]. This gradient of oxygen vacancies (and accordingly of electrons and electron holes) causes an increased average conductivity in STO (resistance degradation) [33–36]. This is essentially a redistribution of defects within the STO bulk, and thus is most probably not strongly affected by the surrounding atmosphere. Based on the known defect mobilities in STO, we may estimate the approximate timescale expected for this process. Oxygen vacancy mobility is much lower than that of electronic defects [30] and thus the motion of oxygen vacancies limits the formation of the stoichiometry gradient. For a rough approximation we may assume that an average oxygen vacancy has to travel a distance on the order of the thickness of the STO crystal to build up the stoichiometry gradient. In accordance with empirical data from Ref. [32] we suppose that under the electric field  $E$ , here induced by the photo-voltage, an oxygen vacancy migrates across a single crystal of thickness  $d$  in the characteristic time

$$t_{\text{ch}} = \frac{d}{v} = \frac{d}{uE} = \frac{d^2}{uU}, \quad (3)$$

where  $v$  and  $u$  are the velocity and mobility of oxygen vacancies. The relevant voltage  $U$  depends on the bulk and space charge resistances and thus changes with time. In the initial phase of stoichiometry polarization, the STO bulk resistance is still larger than the resistance of the illuminated space charge [37], and thus we may estimate  $U$  as the photo-

voltage.

Using a mobility of  $1.72 \times 10^{-6} \text{ cm}^2 \text{ V}^{-1}$  at  $350 \text{ }^\circ\text{C}$  taken from Ref. [30] Eq. (3) we thus obtain a time of 1450 s. This is very close to the characteristic times of the atmosphere independent process (20 to 30 min). Once illumination is removed, this stoichiometry gradient is expected to relax back to the equilibrium concentration profile over the same time span, i.e. 20 to 30 min. This is also consistent with the reoccurrence of the effect I increase after every interruption of the illumination. Thus, process I, i.e. the “rapid” conductivity increase under UV, is indeed most probably caused by stoichiometry polarization.

Additionally, under UV illumination also the oxygen exchange kinetics between STO in the neighboring phase is modified due to modified electron and electron hole concentrations in the light absorbing region. This results in quasi-Fermi levels of electrons and holes, and thus also to a splitting of the oxygen chemical potential into two quasi-chemical potentials. For free STO surfaces, this accelerates the incorporation of oxygen into the STO crystal [19,38], and thus leads to a photo-oxidation and ultimately to an increase of the oxygen chemical potential in the entire STO crystal [15,20,39].

In our case the STO surface is covered by the LSCr layer. In the highly conducting LSC thin film itself, we do not expect strongly changed charge carrier concentrations under UV. However, the UV light reaching the STO crystal strongly changes electron (and electron hole) concentrations and thus causes modified quasi-chemical potentials of oxygen in the illuminated STO region, which transfer to the adjacent LSCr layer

and thus act as a driving force for modified oxygen exchange. Supposed the light induced oxygen chemical potential in STO and thus also in LSCr is such that further oxygen is incorporated, we end up in the same situation as for free STO surfaces, namely a photo-oxidation of STO. Comparing the STO transport resistance of the as-prepared cells to the fully enhanced cells in synthetic air, we may estimate that this photo-oxidation causes an increase in the electron hole concentration by about three orders of magnitude. This is even somewhat larger than in pure photo-oxidation experiments without covering LSCr layer [15,20]. Based on the defect model of STO we estimate that this corresponds to an increase of the equivalent oxygen partial pressure by several orders of magnitude, exact values, however, would require detailed knowledge about the defect chemical system including trap states.

Since this photo-oxidation involves an oxygen incorporation reaction at the LSCr surface, it likely reacts very sensitively to contaminants in the atmosphere, and thus may occur on different timescales in ambient air and in pure, synthetic air. For example, very severe contaminant dependencies of the oxygen exchange reaction are often observed both on closely related perovskites (e.g. LSC,  $\text{La}_{0.6}\text{Sr}_{0.4}\text{FeO}_{3-\delta}$  or  $\text{SrTi}_x\text{Fe}_{1-x}\text{O}_{3-\delta}$ ) and also on fluorite materials such as  $\text{Pr}_x\text{Ce}_{1-x}\text{O}_{2-\delta}$  [40–43]. Very clean synthetic air may thus enable rather fast oxygen incorporation and thus photo-oxidation under illumination, while ambient air strongly retards this process. Without illumination, on the other hand, the oxygen exchange reaction is assumed to be very slow at 350 °C, probably also due to the much more pronounced space charge at the STO-LSCr interface in the dark. This explains the experimental fact of STO crystals remaining highly conductive after illumination for an extended time. Photo-oxidation can thus explain the second self-enhancement process in our HT-PV cells.

## 7. Conclusion

Photo-active heterojunctions between STO single crystals and LSCr thin film photo-electrodes were prepared by PLD and characterized photo-electrochemically. DC measurements of OCV and SCC under UV illumination revealed a pronounced self-enhancement of the SCC by almost an order of magnitude, whereas the OCV remained largely unaffected. Two processes with very different characteristic times and atmosphere dependencies govern this current increase. A first process (20 min) is present in both ambient air and pure synthetic air and is likely caused by a stoichiometry polarization of the STO single crystal due to the photo-voltage dropping across the STO crystal. A second process leading to further changes in the sample is very slow in ambient air (150 h), but strongly accelerated in pure synthetic air. Most likely, it is related to photo-oxidation of the STO crystal under illumination which is retarded in ambient air due to contaminants. Impedance spectroscopy showed that this current enhancement corresponds to a reduction of both main contributors to the cells' internal resistance, i.e. the bulk transport resistance through the STO crystal and the space charge resistance.

After this self-enhancement, such cells produced SCCs of up to 2 mA  $\text{cm}^{-2}$  and power densities up to 130  $\mu\text{W cm}^{-2}$  at 350 °C. EIS under illumination and at different DC bias voltages was used to identify individual loss processes. The total cell resistance is dominated by the resistance of the space charge region at the photo-active junction between STO and LSCr. Consequently, the cell performance is limited by this space charge, whereas the transport through the STO crystal contributes at most 10% to the total losses. This is also a direct consequence of the self-enhancement, which reduces the transport resistance of the STO by over three orders of magnitude and thus renders it negligible. Accordingly, the self-enhancement is triggered by time dependent changes of the bulk (stoichiometry polarization and photo-oxidation), but is finally reflected in the corresponding changes of the space charge resistance.

## CRedit authorship contribution statement

**Alexander Schmid:** Conceptualization, Data curation, Formal analysis, Investigation, Methodology, Project administration, Software, Supervision, Validation, Visualization, Writing – original draft, Writing – review & editing. **Ludwig Enzberger:** Investigation, Methodology. **Jürgen Fleig:** Conceptualization, Funding acquisition, Project administration, Supervision, Writing – review & editing.

## Declaration of competing interest

The authors declare that they have no known competing financial interests or personal relationships that could have appeared to influence the work reported in this paper.

## Data availability

Data will be made available on request.

## Acknowledgements

This project has received funding from the European Union's Horizon 2020 research and innovation programme under grant agreement No 824072 (Harvestore). The authors acknowledge TU Wien Bibliothek for financial support through its Open Access Funding Programme.

## Appendix A. Supplementary data

Supplementary data to this article can be found online at <https://doi.org/10.1016/j.ssi.2024.116469>.

## References

- [1] S. Rühle, A.Y. Anderson, H.-N. Barad, B. Kupfer, et al., All-oxide photovoltaics, *J. Phys. Chem. Lett.* 3 (2012) 3755–3764, <https://doi.org/10.1021/jz3017039>.
- [2] C. Strümpel, M. McCann, G. Beaucarne, V. Arkhipov, et al., Modifying the solar Spectrum to enhance silicon solar cell efficiency — an overview of available materials, *Sol. Energy Mater. Sol. Cells* 91 (2007) 238–249, <https://doi.org/10.1016/j.solmat.2006.09.003>.
- [3] M.A. Green, The path to 25% silicon solar cell efficiency: history of silicon cell evolution, *Prog. Photovolt. Res. Appl.* 17 (2009) 183–189, <https://doi.org/10.1002/ppp.892>.
- [4] A.D. Al-Ghiffari, N.A. Ludin, M.L. Davies, R.M. Yunus, et al., Systematic review of molybdenum disulfide for solar cell applications: properties, mechanism and application, *Mater. Today Commun.* 32 (2022) 104078, <https://doi.org/10.1016/j.mtcomm.2022.104078>.
- [5] M.A. Scarpulla, B. McCandless, A.B. Phillips, Y. Yan, et al., CdTe-based thin film photovoltaics: recent advances, current challenges and future prospects, *Sol. Energy Mater. Sol. Cells* 255 (2023) 112289, <https://doi.org/10.1016/j.solmat.2023.112289>.
- [6] B.P. Rai,  $\text{Cu}_2\text{O}$  solar cells: a review, *Solar Cells* 25 (1988) 265–272, [https://doi.org/10.1016/0379-6787\(88\)90065-8](https://doi.org/10.1016/0379-6787(88)90065-8).
- [7] J. Herion, E.A. Niekisch, G. Scharl, Investigation of metal oxide/cuprous oxide heterojunction solar cells, *Solar Energy Mater.* 4 (1980) 101–112, [https://doi.org/10.1016/0165-1633\(80\)90022-2](https://doi.org/10.1016/0165-1633(80)90022-2).
- [8] T. Minami, Y. Nishi, T. Miyata, J.-I. Nomoto, High-efficiency oxide solar cells with  $\text{ZnO}/\text{Cu}_2\text{O}$  heterojunction fabricated on thermally oxidized  $\text{Cu}_2\text{O}$  sheets, *Appl. Phys. Express* 4 (2011) 062301, <https://doi.org/10.1143/apex.4.062301>.
- [9] D. Li, C.-J. Chien, S. Deora, P.-C. Chang, et al., Prototype of a scalable Core-Shell  $\text{Cu}_2\text{O}/\text{TiO}_2$  solar cell, *Chem. Phys. Lett.* 501 (2011) 446–450, <https://doi.org/10.1016/j.cplett.2010.11.064>.
- [10] T. Dittrich, V. Duzhko, F. Koch, V. Kytin, et al., Trap-limited Photovoltage in ultrathin metal oxide layers, *Phys. Rev. B* 65 (2002) 155319, <https://doi.org/10.1103/physrevb.65.155319>.
- [11] S.Y. Yang, L.W. Martin, S.J. Byrnes, T.E. Conry, et al., Photovoltaic effects in  $\text{BiFeO}_3$ , *Appl. Phys. Lett.* 95 (2009) 062909, <https://doi.org/10.1063/1.3204695>.
- [12] S. Nakashima, T. Uchida, D. Nakayama, H. Fujisawa, et al., Bulk Photovoltaic Effect in a  $\text{BiFeO}_3$  Thin Film on a  $\text{SrTiO}_3$  substrate, *Jpn. J. Appl. Phys.* 53 (2014), <https://doi.org/10.7567/jjap.53.09pa16>, 09PA16.
- [13] M. Siebenhofer, A. Viernstein, M. Morgenbesser, J. Fleig, et al., Photoinduced electronic and ionic effects in strontium Titanate, *Mater. Adv.* 2 (2021) 7583–7619, <https://doi.org/10.1039/d1ma00906k>.
- [14] M.-H. Huang, J.-Y. Xia, Y.-M. Xi, C.-X. Ding, Study on Photochromism in  $\text{SrTiO}_3:\text{Fe}$  Ceramic Powder, *J. Eur. Ceram. Soc.* 17 (1997) 1761–1765, [https://doi.org/10.1016/s0955-2219\(97\)00009-5](https://doi.org/10.1016/s0955-2219(97)00009-5).

- [15] A. Viernstein, M. Kubicek, M. Morgenbesser, G. Walch, et al., High-temperature Photochromism of Fe-doped SrTiO<sub>3</sub> caused by UV-induced bulk stoichiometry changes, *Adv. Funct. Mater.* 29 (2019) 1900196, <https://doi.org/10.1002/adfm.201900196>.
- [16] F. Rossella, P. Galinetto, G. Samoggia, V. Trepakov, et al., Photoconductivity and the structural phase transition in SrTiO<sub>3</sub>, *Solid State Commun.* 141 (2007) 95–98, <https://doi.org/10.1016/j.ssc.2006.09.006>.
- [17] H. Katsu, H. Tanaka, T. Kawai, Anomalous photoconductivity in SrTiO<sub>3</sub>, *Jpn. J. Appl. Phys.* 39 (2000) 2657, <https://doi.org/10.1143/jjap.39.2657>.
- [18] F.V.E. Hensling, D.J. Keeble, J. Zhu, S. Brose, et al., UV radiation enhanced oxygen vacancy formation caused by the PLD plasma plume, *Sci. Rep.* 8 (2018) 8846, <https://doi.org/10.1038/s41598-018-27207-5>.
- [19] R. Merkle, R.A. De Souza, J. Maier, Optically tuning the rate of stoichiometry changes: surface-controlled oxygen incorporation into oxides under UV irradiation, *Angew. Chem. Int. Ed.* 40 (2001) 2126–2129, [https://doi.org/10.1002/1521-3773\(20010601\)40:11<2126::aid-anie2126>3.0.co;2-k](https://doi.org/10.1002/1521-3773(20010601)40:11<2126::aid-anie2126>3.0.co;2-k).
- [20] A. Viernstein, M. Kubicek, M. Morgenbesser, T.M. Huber, et al., Mechanism of Photoionic stoichiometry changes in SrTiO<sub>3</sub>, *Solid State Ionics* 383 (2022) 115992, <https://doi.org/10.1016/j.ssi.2022.115992>.
- [21] M. Siebenhofer, T. Huber, W. Artner, J. Fleig, et al., Substrate stoichiometry changes during pulsed laser deposition: a case study on SrTiO<sub>3</sub>, *Acta Mater.* 203 (2021) 116461, <https://doi.org/10.1016/j.actamat.2020.10.077>.
- [22] F.X. Hao, C. Zhang, X. Liu, Y.W. Yin, et al., Photovoltaic effect in YBa<sub>2</sub>Cu<sub>3</sub>O<sub>7-δ</sub>/Nb-doped SrTiO<sub>3</sub> heterojunctions, *Appl. Phys. Lett.* 109 (2016) 131104, <https://doi.org/10.1063/1.4963759>.
- [23] J.F. Wang, D. Cao, Y. Zhou, X.Y. Wang, et al., Series Resistance Effects in La<sub>0.5</sub>Sr<sub>0.5</sub>MnO<sub>3</sub>/SrTiO<sub>3</sub>:Nb (001) Heterojunctions, *J. Phys. D: Appl. Phys.* 48 (2015) 385104, <https://doi.org/10.1088/0022-3727/48/38/385104>.
- [24] K. Wang, W. Gao, H.W. Zheng, F.Z. Li, et al., Heteroepitaxial growth of Cu<sub>2</sub>O films on Nb-SrTiO<sub>3</sub> substrates and their photovoltaic properties, *Ceram. Int.* 43 (2017) 16232–16237, <https://doi.org/10.1016/j.ceramint.2017.08.205>.
- [25] M. Morgenbesser, A. Schmid, A. Viernstein, J. de Dios Sirvent, et al., SrTiO<sub>3</sub> Based High Temperature Solid Oxide Solar Cells: Photovoltages, Photocurrents and Mechanistic Insight, *Solid State Ionics* 368 (2021) 115700, <https://doi.org/10.1016/j.ssi.2021.115700>.
- [26] G.C. Brunauer, B. Rotter, G. Walch, E. Esmaeili, et al., UV-light-driven oxygen pumping in a high-temperature solid oxide Photoelectrochemical cell, *Adv. Funct. Mater.* 26 (2015) 120–128, <https://doi.org/10.1002/adfm.201503597>.
- [27] G. Walch, B. Rotter, G.C. Brunauer, E. Esmaeili, et al., A solid oxide Photoelectrochemical cell with UV light-driven oxygen storage in mixed conducting electrodes, *J. Mater. Chem. A* 5 (2017) 1637–1649, <https://doi.org/10.1039/c6ta08110j>.
- [28] M. Siebenhofer, F. Baiutti, J. de Dios Sirvent, T.M. Huber, et al., Exploring point defects and trap states in Undoped SrTiO<sub>3</sub> single crystals, *J. Eur. Ceram. Soc.* 42 (2022) 1510–1521, <https://doi.org/10.1016/j.jeurceramsoc.2021.10.010>.
- [29] R.A. DeSouza, J. Fleig, J. Maier, O. Kienzle, et al., Electrical and structural characterization of a low-angle tilt grain boundary in Iron-doped strontium Titanate, *J. Am. Ceram. Soc.* 86 (2003) 922–928, <https://doi.org/10.1111/j.1151-2916.2003.tb03398.x>.
- [30] I. Denk, W. Münch, J. Maier, Partial conductivities in SrTiO<sub>3</sub>: bulk polarization experiments, oxygen concentration cell measurements, and defect-chemical modeling, *J. Am. Ceram. Soc.* 78 (1995) 3265–3272, <https://doi.org/10.1111/j.1151-2916.1995.tb07963.x>.
- [31] J. Fleig, S. Rodewald, J. Maier, Microcontact impedance measurements of individual highly resistive grain boundaries: general aspects and application to acceptor-doped SrTiO<sub>3</sub>, *J. Appl. Phys.* 87 (2000) 2372–2381, <https://doi.org/10.1063/1.372189>.
- [32] T. Baiatu, R. Waser, K.-H. Härdtl, Dc electrical degradation of perovskite-type Titanates: III, a model of the mechanism, *J. Am. Ceram. Soc.* 73 (1990) 1663–1673, <https://doi.org/10.1111/j.1151-2916.1990.tb09811.x>.
- [33] R. Waser, T. Baiatu, K.-H. Härdtl, Dc electrical degradation of perovskite-type Titanates: I, ceramics, *J. Am. Ceram. Soc.* 73 (1990) 1645–1653, <https://doi.org/10.1111/j.1151-2916.1990.tb09809.x>.
- [34] R. Waser, T. Baiatu, K.-H. Härdtl, Dc electrical degradation of perovskite-type Titanates: II, single crystals, *J. Am. Ceram. Soc.* 73 (1990) 1654–1662, <https://doi.org/10.1111/j.1151-2916.1990.tb09810.x>.
- [35] S. Rodewald, N. Sakai, K. Yamaji, H. Yokokawa, et al., The effect of the oxygen exchange at electrodes on the high-voltage Electrocoloration of Fe-doped strontium single crystals: a combined Sims and microelectrode impedance study, *J. Electroceram.* 7 (2001) 95–105, <https://doi.org/10.1023/a:1013118321456>.
- [36] S. Rodewald, J. Fleig, J. Maier, Resistance degradation of Iron-doped strontium Titanate investigated by spatially resolved conductivity measurements, *J. Am. Ceram. Soc.* 83 (2004) 1969–1976, <https://doi.org/10.1111/j.1151-2916.2000.tb01499.x>.
- [37] M. Morgenbesser, S. Taibl, M. Kubicek, A. Schmid, et al., Cation non-stoichiometry in Fe:SrTiO<sub>3</sub> thin films and its effect on the electrical conductivity, *Nanoscale Adv.* 3 (2021) 6114–6127, <https://doi.org/10.1039/d1na00358e>.
- [38] R. Merkle, J. Maier, Oxygen incorporation into Fe-doped SrTiO<sub>3</sub>: mechanistic interpretation of the surface reaction, *Phys. Chem. Chem. Phys.* 4 (2002) 4140–4148, <https://doi.org/10.1039/b204032h>.
- [39] M. Morgenbesser, A. Viernstein, A. Schmid, C. Herzig, et al., Unravelling the origin of ultra-low conductivity in SrTiO<sub>3</sub> thin films: Sr vacancies and Ti on A-sites cause Fermi level pinning, *Adv. Funct. Mater.* 32 (2022) 2202226, <https://doi.org/10.1002/adfm.202202226>.
- [40] A. Schmid, A. Nennung, A. Opitz, M. Kubicek, et al., High oxygen exchange activity of pristine La<sub>0.6</sub>Sr<sub>0.4</sub>FeO<sub>3-δ</sub> films and its degradation, *J. Electrochem. Soc.* 167 (2020) 124509, <https://doi.org/10.1149/1945-7111/abac2b>.
- [41] M. Siebenhofer, T.M. Huber, G. Friedbacher, W. Artner, et al., Oxygen exchange kinetics and nonstoichiometry of pristine La<sub>0.6</sub>Sr<sub>0.4</sub>CoO<sub>3-δ</sub> thin films unaltered by degradation, *J. Mater. Chem. A* 8 (2020) 7968–7979, <https://doi.org/10.1039/c9ta13020a>.
- [42] C. Riedl, M. Siebenhofer, A. Nennung, A. Schmid, et al., In situ techniques reveal the true capabilities of SOFC cathode materials and their sudden degradation due to omnipresent sulfur trace impurities, *J. Mater. Chem. A* 10 (2022) 14838–14848, <https://doi.org/10.1039/d2ta03335f>.
- [43] S. Kogler, A. Nennung, G.M. Rupp, A.K. Opitz, et al., Comparison of electrochemical properties of La<sub>0.6</sub>Sr<sub>0.4</sub>FeO<sub>3-δ</sub> thin film electrodes: oxidizing vs. reducing conditions, *J. Electrochem. Soc.* 162 (2015) F317–F326, <https://doi.org/10.1149/2.0731503jes>.